

A unified description of the structure and electromagnetic breakup of ^{11}Be

M. Dan,^{1,*} R. Chatterjee,^{1,†} and M. Kimura^{2,3,4,‡}

¹*Department of Physics, Indian Institute of Technology Roorkee, Roorkee 247 667, India*

²*Department of Physics, Hokkaido University, 060-0810 Sapporo, Japan*

³*Nuclear Reaction Data Centre, Faculty of Science, Hokkaido University, 060-0810 Sapporo, Japan*

⁴*Research Center for Nuclear Physics (RCNP), Osaka University, Ibaraki 567-0047, Japan*

We study both the static properties of ^{11}Be and its reaction dynamics during electromagnetic breakup under a unified framework. A many-body approach - the antisymmetrized molecular dynamics (AMD) is used to describe the structure of the neutron-halo nucleus, ^{11}Be . The same AMD wave function is then adapted as an input to the fully quantum theory of Coulomb breakup under the aegis of the finite range distorted wave Born approximation theory. The calculated observables are also compared with those obtained with a phenomenological Woods-Saxon potential model wave function. The experimental core-valence neutron relative energy spectrum and dipole response along with other observables are well described by our calculations.

I. INTRODUCTION

Since the discovery of halo nuclei [1], several observations in their study have shown unconventional results, which were contrary to traditional nuclear structure estimations. For example, unlike the case of stable nuclei where the matter radius generally follow the charge radius, the matter radius of ^{11}Be was found to be larger than its charge radius. The full width at half-maximum (FWHM) of the parallel momentum distribution (PMD) of stable nuclei (≈ 140 MeV/c) is much higher compared to that from a halo nucleus (≈ 40 MeV/c). For $^{10,11,12}\text{Be}$ breaking up on a heavy target (Au), the FWHM of the PMD of the charged fragment are 191.13 MeV/c, 43.23 MeV/c and 88.93 MeV/c, respectively [2].

It is generally considered that a large neutron to proton ratio results in a sharp decrease of the one-neutron separation energy, and consequently an extension in the neutron wave function far outside the nuclear mean field is observed [3]. This extension directly affects the static properties of the system. The root mean square matter radius of ^{10}Be and ^{11}Be are 2.30 ± 0.02 fm and 2.73 ± 0.05 fm, respectively [4]. In a neutron halo nucleus, one can get information on the interaction between the clusters of a dicluster nucleus from the change of nuclear charge distribution. These changes may occur due to the relative motion between the core and the centre of mass, and due to the core polarization resulting from the core-valence neutron interaction [5]. There are several studies [6–9] that report on charge and matter radius of ^{11}Be . However more analysis are required for a consistent picture. The comparison between charge and matter radii is significant for the nuclei with different distribution of neutron and proton halo.

Tanihata *et. al.* [1] have shown that there is a notable increase in interaction cross section for drip line nuclei

compared to the neighbouring isotopes of light elements. There is an increase in one neutron removal cross section (σ_n) for ^{11}Be as compared to ^{10}Be , while breaking up on a Pb target. The average one neutron removal cross section for ^{10}Be (beam energy ranging from 37 - 70 MeV/u) is 0.126 ± 0.011 b, while that for ^{11}Be (beam energy ranging from 17 - 66 MeV/u), is 2.16 ± 0.17 b [10]. It is evident that the average one neutron removal cross section of ^{11}Be is an order of magnitude higher than that of ^{10}Be . The unusually large reaction cross section of a halo nuclei, compared to its isobars, is a consequence of the matter radius significantly deviating from the usual $A^{1/3}$ dependence expected for stable nuclei [11].

The analysis of an external nuclear or electromagnetic field response by a nucleus is one of the key elements to understand the characteristics of a many-body nuclear system [12]. At present, there are several discussions about the way giant dipole resonance strength evolves from stable to weakly bound exotic nuclei in extreme neutron to proton ratios. In general, the presence of collective soft-dipole resonance is expected to occur in heavier neutron-rich structures at excitation energies lower than the giant dipole resonance [13, 14]. Such a mode may arise when loosely bound valence neutrons vibrate against the residual core. In the literature, it is often referred to as pygmy resonance. In electromagnetic dissociation experiments (*e.g.* [15, 16]), a prominent low-lying dipole strength was observed in light halo nucleus. Their presence is justified by two arguments: first is due to the coherent vibration of two halo neutrons against the charge core (*e.g.* ^6He [17] and ^{11}Li [18]) and second is due to the non-resonant breakup of one neutron halo nucleus (*e.g.* ^{11}Be [15] and ^{19}C [16]) into the continuum [12, 19, 20]. It is also reported that astrophysical aspects such as abundance pattern in the r-process nucleosynthesis could also be related to the presence of low-lying dipole strength present in neutron-rich nuclei [21, 22].

In this article, we aim to combine nuclear structure and reaction models to discuss both the static and dynamical properties of a neutron-halo nucleus, ^{11}Be . For this purpose, we use the antisymmetrized molecular dynamics (AMD) [23–25] to calculate the static properties

* mdan@ph.iitr.ac.in

† rchatterjee@ph.iitr.ac.in

‡ masaaki@nucl.sci.hokudai.ac.jp

such as one neutron separation energy, charge and matter radii. The AMD wave function is also used as an input to the fully quantum mechanical Coulomb breakup theory of finite range distorted wave Born approximation (FRDWBA) to calculate several reaction observables in the breakup of ^{11}Be on a heavy target (^{208}Pb) such as triple differential cross section, neutron energy distribution, parallel momentum distribution, relative energy spectrum, and dipole response of ^{11}Be . The results are also compared with the available experimental data, and also with those obtained from a phenomenological wave function derived using a Woods-Saxon (WS) potential whose depth is adjusted to fit the one neutron separation energy of ^{11}Be .

In the following section, a brief description of the FRDWBA theory and details of the AMD framework are presented. The results and analysis from our calculations have been discussed in section 3, wherein we present the static properties of ^{11}Be followed by calculations of various reaction observables in during its electromagnetic breakup on a heavy target. The conclusions of our work appear in section 4.

II. FORMULATION

A. Framework of FRDWBA

If we assume a projectile ‘ a ’ (^{11}Be), consisting of substructures ‘ b ’ (^{10}Be) and ‘ c ’ (neutron) to breakup in the pure Coulomb field of a heavy target ‘ t ’ (^{208}Pb). Then, the triple differential cross section for the process $a + t \rightarrow b + c + t$ can be written as,

$$\frac{d^3\sigma}{dE_b d\Omega_b d\Omega_c} = \frac{2\pi}{\hbar v_{at}} \rho(E_b, \Omega_b, \Omega_c) \sum_{l,m} |\beta_{lm}|^2, \quad (1)$$

where, v_{at} is the relative velocity between the a - t system in the entrance channel, $\rho(E_b, \Omega_b, \Omega_c)$ is the three body final state phase space factor [26]. The reduced transition amplitude in the post form FRDWBA, β_{lm} , for the breakup process is given by [27],

$$\beta_{lm}(\mathbf{q}_b, \mathbf{q}_c; \mathbf{q}_a) = \left\langle \zeta_b^{(-)}(\mathbf{q}_b, \mathbf{r}) \zeta_c^{(-)}(\mathbf{q}_c, \mathbf{r}_c) \Big| V_{bc}(\mathbf{r}_1) \right. \\ \left. \times \Big| \phi_a^{lm}(\mathbf{r}_1) \zeta_a^{(+)}(\mathbf{q}_a, \mathbf{r}_i) \right\rangle. \quad (2)$$

ζ_i 's ($i = a, b, c$) are the pure Coulomb distorted waves of the appropriate particles with respect to the target and \mathbf{q}_i 's are the associated Jacobi wave vectors. The position vectors are shown in Fig. 1 with $\mathbf{r} = \mathbf{r}_i - \alpha\mathbf{r}_1$ and $\mathbf{r}_c = \gamma\mathbf{r}_1 + \delta\mathbf{r}_i$, where α , γ and δ are the mass factors: $\alpha = m_c/(m_c + m_b)$; $\gamma = m_t/(m_b + m_t)$; $\gamma = (1 - \alpha\delta)$ and m_i 's ($i = b, c, t$) are the masses of the appropriate particles.

$\phi_a^{lm}(\mathbf{r}_1)$ is the ground state wave function of the projectile (a), which is an eigenfunction of the two-body bound state potential $V_{bc}(\mathbf{r}_1)$, with l and m as the orbital angular momentum and its projection, respectively. Other

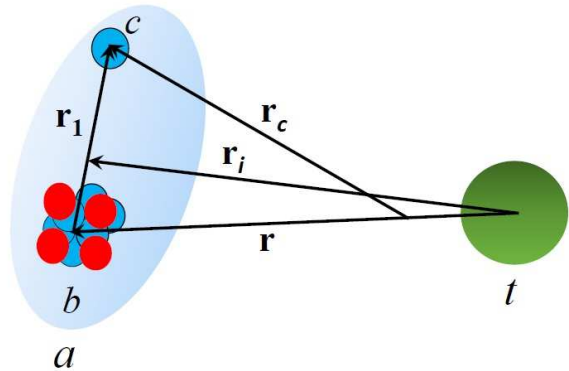


FIG. 1. The three body Jacobi coordinate system. The corresponding position vectors are denoted by \mathbf{r} 's.

reaction observables such as relative energy spectrum, neutron energy distribution, and parallel momentum distribution can be calculated by suitably integrating Eq. (1). The dipole strength distribution $dB(E1)/dE$ can be obtained [28] from the relative energy spectra $d\sigma/dE_{rel}$ using

$$\frac{d\sigma}{dE_{rel}} = \frac{16\pi^3}{9\hbar c} n_{E1} \frac{dB(E1)}{dE}, \quad (3)$$

where, n_{E1} is the virtual photon number for electric dipole transition. For more details of the theory one is referred to [27].

The main input to this theory is the wave function $\phi_a^{lm}(\mathbf{r}_1) = u_l(r_1) Y^{lm}(\hat{\mathbf{r}}_1)$, or more specifically the bound state radial wave function $u_l(r_1)$. In this work, we test two different approaches to calculate this primary structure input to the theory. An ordinary option is to calculate $u_l(r_1)$ from the core-valence neutron interaction with the WS form whose depth is adjusted to reproduce the one-neutron separation energy with fixed radius and diffuseness parameters. An alternative and more sophisticated approach would be to use $u_l(r_1)$ derived from a microscopic many-body wave function of the AMD, which is discussed in details in the next section.

B. Model for the structure calculation

The framework of AMD and the method to calculate valence neutron wave function (overlap amplitude) are briefly explained. For more details, readers are directed to Refs. [23–25].

1. Framework of AMD

The Hamiltonian used in this study is given as,

$$H = \sum_{i=1}^A t(i) + \sum_{i<j}^A v_n(ij) + \sum_{i<j}^Z v_C(ij) - t_{cm}, \quad (4)$$

where, the Gogny D1S interaction [29] is used as an effective nucleon-nucleon interaction v_n . Following the prescription made in Ref. [30], we have weakened the strength of the spin-orbit interaction by 5% from the original one to reproduce the observed splitting of the $1/2^\pm$ states of ^{11}Be . The Coulomb interaction, v_C is approximated by a sum of seven Gaussians, and the center-of-mass kinetic energy, t_{cm} is exactly removed.

The intrinsic wave function, Φ_{int} is represented by a Slater determinant of single-particle wave packets. It is projected to the eigenstate of parity before the variation (parity projection before variation).

$$\Phi_{int} = \mathcal{A}\{\varphi_1\varphi_2 \cdots \varphi_A\}, \quad (5)$$

$$\Phi_{int}^\pi = P^\pi \Phi_{int} = \frac{1 + \pi \hat{P}_x}{2} \Phi_{int}, \quad (\pi = \pm), \quad (6)$$

where, P^π and P_x denote the parity projector and parity operator, respectively. The single-particle wave packet, φ_i has the deformed Gaussian form [31],

$$\varphi_i(\mathbf{r}) = \prod_{\sigma=x,y,z} (2\nu_\sigma/\pi)^{1/4} \exp\{-\nu_\sigma(r_\sigma - Z_{i\sigma})^2\} \chi_i \eta_i, \quad (i = 1, 2, \dots, A). \quad (7)$$

χ_i is the nucleon spinor and η_i is the isospin fixed to either of proton or neutron. The parameters of the wave function (\mathbf{Z}_i , ν and χ_i) are determined by the energy variation which minimizes the expectation value of the Hamiltonian,

$$H = \frac{\langle \Phi^\pi | H | \Phi^\pi \rangle}{\langle \Phi^\pi | \Phi^\pi \rangle} + v_\beta (\langle \beta \rangle - \beta)^2. \quad (8)$$

Note that the potential $v_\beta (\langle \beta \rangle - \beta)^2$ imposes the constraint on the quadrupole deformation parameter $\langle \beta \rangle$ defined in Ref. [32]. The magnitude of v_β is chosen large enough so that $\langle \beta \rangle$ equals to β . By the energy variation, we obtain the optimized wave function for each given value of β , which are denoted by $\Phi_{int}^\pi(\beta)$. No constraint was imposed on the other quadrupole deformation parameter γ , and hence, it always has the optimal value.

2. The generator coordinate method and AMD plus resonating group method

To describe the ground and excited states, we perform the angular momentum projection and the generator coordinate method. The optimized wave functions $\Phi_{int}^\pi(\beta)$

are projected to the eigenstates of the total angular momentum,

$$\begin{aligned} \Phi_{MK}^{J\pi}(\beta) &= P_{MK}^J \Phi_{int}^\pi(\beta) \\ &= \frac{2J+1}{8\pi^2} \int d\Omega D_{MK}^{J*}(\Omega) R(\Omega) \Phi_{int}^\pi(\beta), \end{aligned} \quad (9)$$

where, P_{MK}^J , $D_{MK}^J(\Omega)$ and $R(\Omega)$ denote the angular momentum projector, the Wigner D function and the rotation operator, respectively. The integrals over three Euler angles Ω are evaluated numerically. Then, we superpose the wave functions with different quadrupole deformation β and projection of angular momentum K (GCM),

$$\Psi_{M\alpha}^{J\pi} = \sum_{K=-J}^J \sum_{i=1}^N e_{K i \alpha} \Phi_{MK}^{J\pi}(\beta_i), \quad (10)$$

where, N is a number of the basis wave functions to be superposed. The coefficients $e_{K i \alpha}$ and eigenenergy $E_\alpha^{J\pi}$ are obtained by solving the Hill-Wheeler equation [33],

$$\sum_{K'i'} H_{K i K' i'}^{J\pi} e_{K' i' \alpha} = E_\alpha^{J\pi} \sum_{K'i'} N_{K i K' i'}^{J\pi} e_{K' i' \alpha}, \quad (11)$$

$$H_{K i K' i'}^{J\pi} = \langle \Phi_{MK}^{J\pi}(\beta_i) | H | \Phi_{MK'}^{J\pi}(\beta_{i'}) \rangle, \quad (12)$$

$$N_{K i K' i'}^{J\pi} = \langle \Phi_{MK}^{J\pi}(\beta_i) | \Phi_{MK'}^{J\pi}(\beta_{i'}) \rangle. \quad (13)$$

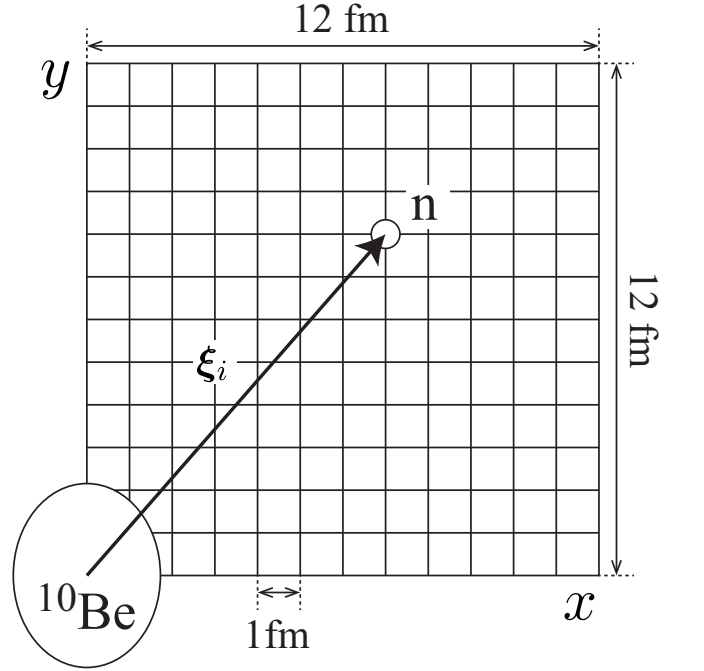


FIG. 2. A schematic illustration of the basis wave function for the $^{10}\text{Be} + n$ system used in the AMD+RGM method.

As explained later, the basis wave functions $\Phi_{MK}^{J\pi}(\beta_i)$ generated by the energy variation are not sufficient to describe the neutron halo of ^{11}Be . To incorporate with the proper asymptotics of the halo wave function, we have introduced a set of wave functions as additional basis. As schematically illustrated in Fig. 2, we have generated the

$^{10}\text{Be} + n$ wave functions by placing the ^{10}Be and n on the grid points within the 12 fm \times 12 fm size with 1 fm intervals. These wave functions may be represented as,

$$\Phi(\xi_i, \chi_n) = \mathcal{A} \left\{ \Phi_{^{10}\text{Be}} \left(-\frac{1}{11} \xi_i \right) \varphi_n \left(\frac{10}{11} \xi_i, \chi_n \right) \right\}. \quad (14)$$

Here, the wave function of ^{10}Be is the intrinsic wave function [Eq. (6)] obtained by the energy variation without constraint on the deformation parameter β , and the valence neutron is described by a Gaussian wave packet [Eq. (7)] placed at $10/11\xi_i$. Because $\Phi_{^{10}\text{Be}}$ has approximate axial and reflection symmetry, the relative coordinate ξ_i between ^{10}Be and the valence neutron can be restricted within the first quadrant of the xy -plane where the y -axis is the symmetry axis of $\Phi_{^{10}\text{Be}}$. Consequently, we have generated $13 \times 13 \times 2 = 338$ basis wave functions (number of grid points \times neutron spin), which are superposed after the angular momentum projection,

$$\Psi_{M\alpha}^{J\pi} = \sum_{K=-J}^J \left\{ \sum_{i=1}^N e_{K i \alpha} \Phi_{MK}^{J\pi}(\beta_i) + \sum_{i=1}^{169} \sum_{\chi_n=\uparrow, \downarrow} f_{K i \chi_n \alpha} P_{MK}^J P^\pi \Phi(\xi_i, \chi_n) \right\}. \quad (15)$$

The coefficients $e_{K i \alpha}$, $f_{K i \chi_n \alpha}$ and eigenenergy $E_\alpha^{J\pi}$ are determined by solving the Hill-Wheeler equation again. We note that this method named AMD plus resonating group method (AMD+RGM) has already been used to describe neutron halo of ^{31}Ne [34–36].

3. Calculation of the valence neutron wave function

We have extracted the valence neutron wave function (overlap amplitude) from the microscopic wave functions of ^{10}Be and ^{11}Be . For this purpose, firstly, we calculate the overlap between the wave functions of ^{10}Be and ^{11}Be .

$$\psi(\mathbf{r}) = \sqrt{11} \left\{ \Psi_M^{J\pi} (^{10}\text{Be}) | \Psi_{M'}^{1/2^+} (^{11}\text{Be}) \right\}. \quad (16)$$

For simplicity, we assume that the wave functions of $^{10,11}\text{Be}$ are described by the parity- and angular-momentum-projected wave functions given by Eq. (9). Then, Eq. (16) reads,

$$\psi(\mathbf{r}) = \sum_{jl} C_{JM, jM' - M}^{1/2M'} u_{jl}(r) / r [Y_l(\hat{r}) \otimes \chi]_{jM' - M} \quad (17)$$

where, the overlap amplitude $u_{jl}(r)$ is defined as,

$$u_{jl}(r) = \sum_k C_{JK' - k, jk}^{1/2K'} \sum_{p=1}^{11} (-)^p r \varphi_{jlk}^{(p)}(r) \times \frac{2J+1}{8\pi^2} \int d\Omega D_{KK' - k}^J(\Omega) \det B^{(p)}(\Omega). \quad (18)$$

Here, $\varphi_{jlk}^{(p)}$ is the multi-pole decomposition of the single-particle wave packet [Eq. (7)],

$$\varphi_p(\mathbf{r}) = \sum_{jlk} \varphi_{jlk}^{(p)}(r) [Y_l(\hat{r}) \otimes \chi]_{jlk}. \quad (19)$$

$\det B^{(p)}(\Omega)$ is the determinant of the sub-matrix $B^{(p)}$ formed by removing p th column from $B(\Omega)$. And $B(\Omega)$ is the (10×11) -dimension overlap matrix between ^{10}Be and ^{11}Be , that is defined as $B(\Omega)_{ij} = \langle \phi_i | R(\Omega) | \varphi_j \rangle$ where ϕ_i and φ_j are being the single-particle wave packets of ^{10}Be and ^{11}Be , respectively. Once the overlap amplitude is calculated, its integral yields the spectroscopic factor,

$$S_{jl} = \int_0^\infty dr |u_{jl}(r)|^2. \quad (20)$$

The derivation of the above formulae is explained in Ref. [37]. It is straightforward to extend them to the GCM and AMD+RGM wave functions given by Eqs. (10) and (15).

III. RESULTS AND DISCUSSIONS

A. Static properties of ^{11}Be

Fig. 3 shows the density profile of the ^{10}Be and ^{11}Be intrinsic wave functions [Eq. (6)] which are obtained by the energy variation and are the dominant components of the ground state. As clearly seen, both nu-

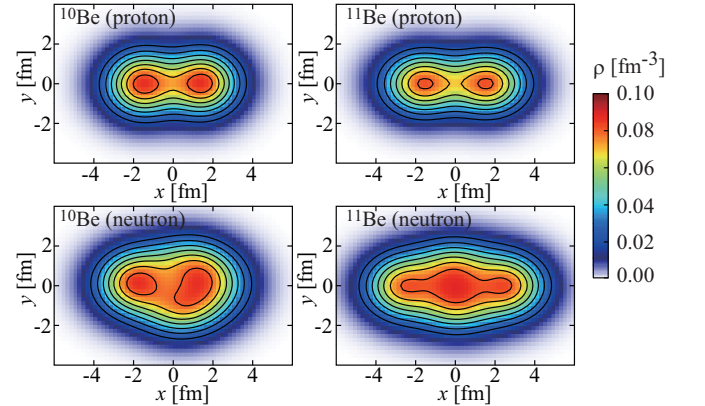


FIG. 3. The proton and neutron density distributions calculated from the intrinsic wave functions which are the dominant component of the ground state. Upper (lower) panels show the proton (neutron) densities.

clei have dumbbell-shaped proton density distributions which indicate the pronounced $\alpha + \alpha$ clustering. The valence neutrons (two valence neutrons of ^{10}Be and three of ^{11}Be) occupy the so-called “molecular orbits” which are the single-particle orbits formed around $\alpha + \alpha$ cluster core [38–41]. In both nuclei, two valence neutrons occupy the π -orbit, and the last valence neutron of ^{11}Be

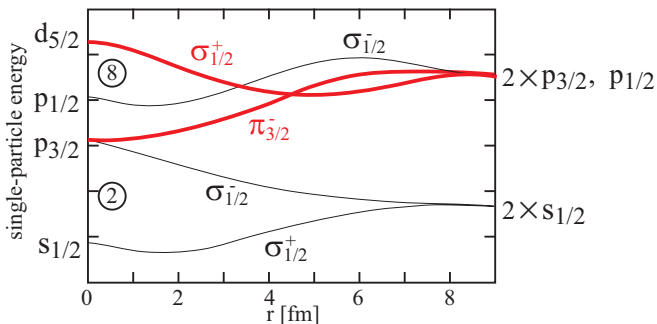


FIG. 4. Schematic figure showing the behavior of the molecular orbits of $\alpha+\alpha$ cluster system as function of the inter-cluster distance. The orbits plotted with red lines show the molecular orbits (π - and σ -orbits) relevant to the low-lying states of ^{10}Be and ^{11}Be . This figure is reconstructed from Fig. 1 of Ref. [39].

occupies the σ -orbit. These molecular-orbit configurations are often denoted as π^2 (^{10}Be) and $\pi^2\sigma$ (^{11}Be). As discussed in Refs. [38–45], the π -orbit reduces the $\alpha + \alpha$ clustering, while the σ -orbit enhances it. This feature originates in the single-particle energies of the molecular orbits as function of the inter-cluster distance illustrated in Fig. 4. The single-particle energy of the π -orbit (σ -orbit) decreases (increases) as function of the inter-cluster distance. As a result, the π -orbit (σ -orbit) favors weaker (stronger) $\alpha + \alpha$ clustering. Since, ^{11}Be has an additional neutron in the σ -orbit, it manifests more pronounced $\alpha + \alpha$ clustering than ^{10}Be as seen in its proton density distribution (Fig. 3) and larger quadrupole deformation parameter (Table I). These characteristics of ^{10}Be and ^{11}Be qualitatively agree with those discussed in the preceding studies [42–46]. We also note that the σ -orbit is a linear combination of the spherical sd -shells, and hence, the valence neutron wave function (overlap amplitude) of ^{11}Be should be, in general, an admixture of the $l = 0$ and 2 components.

Fig. 5 shows the excitation spectra of ^{10}Be and ^{11}Be obtained by the GCM calculations (denoted as AMD in the figure). Contradictory to the observation, the adopted effective interaction does not bound ^{11}Be , although it gives the correct order of the $1/2^\pm$ doublet and other excited states of ^{11}Be . The shortage of the binding energy is due to the insufficient description of the asymptotics of the valence neutron wave function by the AMD framework. The s -wave valence neutron wave function shown in Fig. 6 (black dotted line) decays at short distance and does not show halo nature, reflecting the fact that the AMD framework approximates the valence neutron wave function by a single Gaussian. As a result, neither of the binding nor large matter radius of ^{11}Be are reproduced [4].

To overcome this problem, we have performed the AMD+RGM calculation which superposes the Gaussian wave packets to describe the asymptotics of neutron halo. Fig. 6 shows how the AMD+RGM drasti-

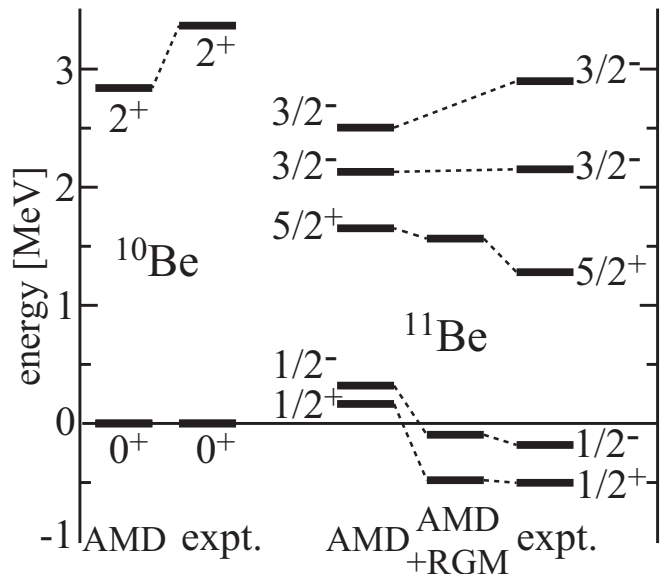


FIG. 5. The calculated and observed excitation spectra of ^{10}Be and ^{11}Be . The energy is relative to the ground state of ^{10}Be .

cally improves the results. The asymptotics of the s -wave ($^{10}\text{Be}(0^+) \otimes s_{1/2}$ channel) is greatly extended toward outside of the core nucleus, and the neutron distribution radius is considerably increased compared to that calculated by AMD (Table I). On the contrary, the asymptotics of the d -wave ($^{10}\text{Be}(2^+) \otimes d_{3/2}$ and $^{10}\text{Be}(2^+) \otimes d_{5/2}$ channels) do not change significantly. This may be due to the centrifugal barrier in these channels which prevents the long-ranged stretched asymptotics. Thanks to the improved asymptotics, the kinetic energy of the halo orbit is reduced and the calculated one-neutron separation energy is now comparable with the observed value.

An interesting side effect brought about by the AMD+RGM is the reduction of the core deformation and the decoupling between the core and valence neutron. As listed in Table I, the quadrupole deformation of the proton distribution decreases in the AMD+RGM result ($\beta_p=0.65$) compared to that of AMD ($\beta_p=0.70$). This implies that the coupling between the core (^{10}Be) and the valence neutron is weakened, and the core polarization decreases. Indeed, in the AMD+RGM result, the spectroscopic factor of the s -wave increases, while that of the d -wave decreases compared to the AMD results. Thus, the AMD+RGM framework brings about a remarkable improvement of the neutron wave function and offers a reasonable description of the neutron halo of ^{11}Be with the deformed core nucleus ^{10}Be . It is also noted that the overlap amplitudes obtained by the AMD+RGM (Fig. 6) look consistent with those obtained by an ab-initio calculations [9, 47, 48].

TABLE I. The calculated and observed one-neutron separation energy (S_n), charge and point nucleon distribution radii ($\sqrt{\langle r_{ch}^2 \rangle}$ and $\sqrt{\langle r_m^2 \rangle}$). The second and third rows shows the results obtained by AMD and AMD+RGM calculations, respectively. The calculated point neutron distribution radii ($\sqrt{\langle r_n^2 \rangle}$) and the quadrupole deformation parameter for proton and neutron (β_p and β_n) are also tabulated. The proton finite size effect is taken into account for the charge radii, while it is not for the neutron and matter radii.

	AMD(+RGM)						expt.		
	S_n (MeV)	$\sqrt{\langle r_{ch}^2 \rangle}$ (fm)	$\sqrt{\langle r_m^2 \rangle}$ (fm)	$\sqrt{\langle r_n^2 \rangle}$ (fm)	β_p	β_n	S_n (MeV)	$\sqrt{\langle r_{ch}^2 \rangle}$ (fm)	$\sqrt{\langle r_m^2 \rangle}$ (fm)
^{10}Be	6.21	2.43	2.35	2.42	0.60	0.56	6.81	2.355(17)	2.30(2)
^{11}Be	-0.22	2.54	2.59	2.71	0.70	0.69	0.50	2.463(15)	2.73(5)
	0.48	2.55	2.71	2.89	0.65	0.62			

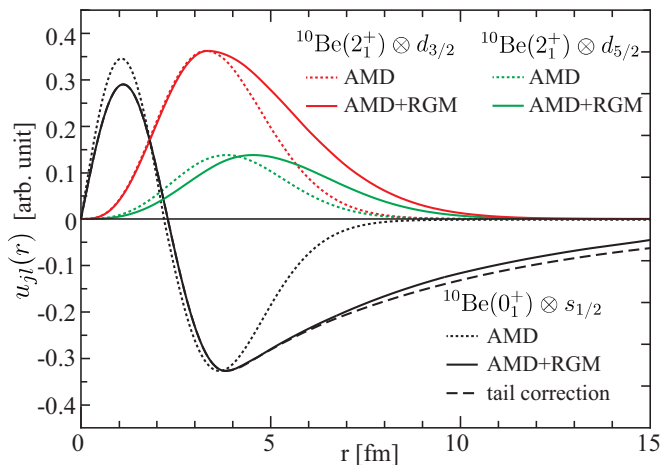


FIG. 6. The overlap amplitudes of the valence neutron of ^{11}Be calculated by the AMD and AMD+RGM. The amplitude is arbitrary scaled for the presentation.

For later use, we further improved the asymptotics of the valence neutron wave function to be consistent with the observed one-neutron separation energy, $S_n = 0.50$ MeV. The s -wave overlap function $u_0(r)$ calculated from AMD+RGM is smoothly connected to the exact asymptotics of $A \exp(-\kappa r)$ where $\kappa = \sqrt{2\mu S_n}/\hbar$ and μ is being the reduced mass for $^{10}\text{Be} + n$ system. The amplitude A and the matching distance a are determined from the condition,

$$\left. \frac{d}{dr} u_0(r) \right|_{r=a} = \left. \frac{d}{dr} A \exp(-\kappa r) \right|_{r=a}. \quad (21)$$

The overlap function with the tail correction, thus obtained, is shown by the dashed line in Fig. 6. This overlap function is used as an input to calculate various reaction observables in the breakup of ^{11}Be on a heavy target in the subsequent sections.

1. Wave function inputs for reaction calculations

The bound state, single-particle radial wave function of ^{11}Be has been built from a $^{10}\text{Be}(0^+) \otimes 1s_{1/2}\nu$ configuration with a one neutron separation energy (S_n) of 0.50 MeV. It is also known that the contribution from the d -wave configuration is an order of magnitude lower than the s -wave and so any admixture (along with a low spectroscopic factor, *cf.* Table II) would not be perceptible in reaction observables (see e.g. Refs. [15, 49, 50]).

The bound state radial wave function of ^{11}Be was constructed in two ways. The first by considering a Woods-Saxon potential of 70.99 MeV, radius and diffuseness parameters as 1.15 fm and 0.50 fm, respectively, so as to reproduce the one-neutron separation energy of 0.50 MeV. The other is by using the overlap wave function obtained by the AMD + RGM framework with tail correction, as described earlier. In all subsequent sections we refer to this wave function as the AMD wave function itself. The two wave functions are compared in Fig. 7. The solid and dashed lines show the phenomenological WS and the microscopic AMD wave functions, respectively.

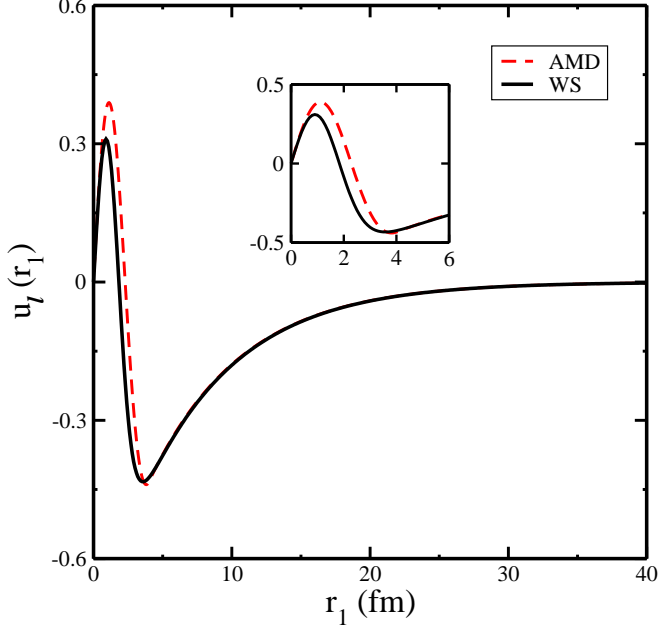
2. Matter and charge radii in the cluster model

It will be interesting to calculate the matter and charge radii in the cluster model [53], with the phenomenological WS and AMD wave functions as inputs and compare them with those obtained in the previous section (Table I). The mean square matter radius $\langle r^2 \rangle_{A_a}$ and charge radius $\langle r_{ch}^2 \rangle_{A_a}$ of a dicluster nucleus of mass number A_a and charge Z_a (consisting of subclusters A_b, Z_b and A_c, Z_c) can be written as [53]

$$\langle r^2 \rangle_{A_a} = \frac{A_b}{A_a} \langle r^2 \rangle_{A_b} + \frac{A_c}{A_a} \langle r^2 \rangle_{A_c} + \frac{A_b * A_c}{A_a^2} \langle R^2 \rangle, \quad (22)$$

TABLE II. The calculated spectroscopic factors which are obtained from the integral of the overlap amplitudes shown in Fig. 6.

channel	AMD	AMD+RGM	expt.
$^{10}\text{Be}(0_1^+) \otimes s_{1/2}$	0.46	0.82	1.0(2) [15], 0.77 [51], 0.74 [3], 0.72(4) [52]
$^{10}\text{Be}(2_1^+) \otimes d_{3/2}$	0.38	0.18	0.18 [3]
$^{10}\text{Be}(2_1^+) \otimes d_{5/2}$	0.11	0.06	

FIG. 7. The normalized bound state radial wave functions of ^{11}Be in WS (solid line) and AMD (dashed line) models. The inset shows the wave functions in the nuclear interior.

and

$$\langle r_{ch}^2 \rangle_{A_a} = \frac{Z_b}{Z_a} \langle r^2 \rangle_{A_b} + \frac{Z_c}{Z_a} \langle r^2 \rangle_{A_c} + \frac{\langle R^2 \rangle}{Z_a} \left(Z_b \cdot \left(\frac{A_c}{A_a} \right)^2 + Z_c \cdot \left(\frac{A_b}{A_a} \right)^2 \right), \quad (23)$$

respectively. In Eqs. (22) and (23), $\langle R^2 \rangle = \langle u_l(r_1) | r_1^2 | u_l(r_1) \rangle$.

In our case, b and c are the core (^{10}Be) and the valence neutron of the projectile respectively. If we neglect the second term of Eq. (22), then the mean square matter radius can be written as

$$\langle r^2 \rangle_{A_a} = \frac{A_b}{A_a} \langle r^2 \rangle_{A_b} + \frac{A_b * A_c}{A_a^2} \langle R^2 \rangle. \quad (24)$$

Furthermore, given that $Z_c = 0$, the mean square charge radius simplifies to

$$\langle r_{ch}^2 \rangle_{A_a} = \frac{Z_b}{Z_a} \langle r^2 \rangle_{A_b} + \frac{\langle R^2 \rangle}{Z_a} \left(Z_b \cdot \left(\frac{A_c}{A_a} \right)^2 \right). \quad (25)$$

For our calculations, we have used the size of the charged core, $\sqrt{\langle r^2 \rangle_{A_b}} = 2.28$ fm. [55]. Evidently, the

TABLE III. Root mean square matter ($\sqrt{\langle r^2 \rangle_{A_a}}$) and charge ($\sqrt{\langle r_{ch}^2 \rangle_{A_a}}$) radii of ^{11}Be in the cluster model.

	WS (fm)	AMD (fm)	expt. (fm)
$\sqrt{\langle r^2 \rangle_{A_a}}$	2.79	2.78	2.73(0.05)[4]
$\sqrt{\langle r_{ch}^2 \rangle_{A_a}}$	2.35	2.35	2.463(15)[54]

WS and the AMD wave functions directly enter the calculation of the radii only through $\langle R^2 \rangle$ term in Eqs. (24 - 25). Thus any difference between the phenomenological WS wave function and the microscopic AMD will be reflected in $\langle R^2 \rangle$. We have also used a spectroscopic factor of 0.82 (in Table II), obtained in the structural calculations shown earlier.

In Table 3, we show that our calculated root mean square matter and charge radii using both the WS and AMD wave functions compare well with the available data. The matter radius calculated from other models such as relativistic mean field model (2.52 fm [6]), Glauber model (2.76(0.03) fm [7]), and fermionic molecular dynamics model (2.80 fm [8]) also agree well with our results. Similarly, the charge radius deduced from the fermionic molecular dynamics (2.38 fm [8]) and no core shell model (2.37(11) fm [9]) agree well with the WS and AMD results.

B. Reaction observables

1. Triple differential cross section

In Fig. 8 we plot the triple differential cross sections in the breakup of ^{11}Be on ^{197}Au target at a beam energy of 44 MeV/nucleon as a function of the neutron energy (E_n), for four different combinations of the neutron angle (θ_n) and the angle of the charged fragment (θ_b). Given that the spectroscopic factor of the s-wave is close to unity [3, 15, 51, 52], our subsequent breakup calculations also take it as unity.

As expected the cross sections are indeed larger at small scattering angles as the breakup is Coulomb dominated. We observe that the calculations obtained from both the WS and AMD wave functions are similar. Given that triple differential cross sections are exclusive reaction observables, this similarity in results builds up an expectation that other reaction observables may also not

be too different while using these wave functions. This is because other inclusive reaction observables can be obtained from the triple differential cross section after performing suitable integrations over various kinematic parameters.

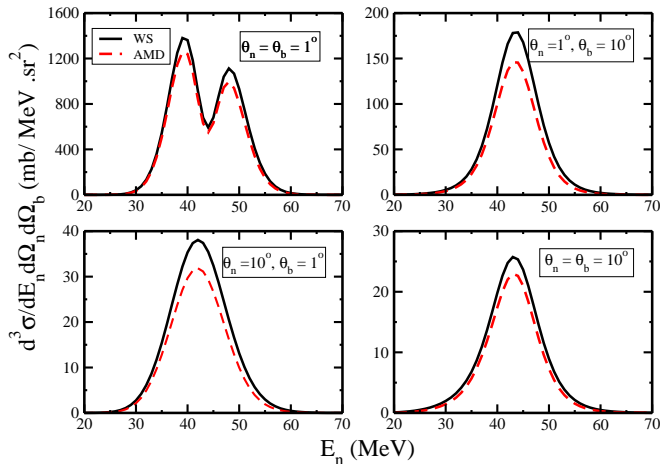


FIG. 8. Triple differential cross section for the breakup of ^{11}Be on ^{197}Au at a beam energy of 44 MeV/nucleon. The solid and dashed lines correspond to WS and AMD calculations, respectively. For more details see text.

2. Neutron energy distribution

We now calculate the neutron energy distribution in the breakup of ^{11}Be on ^{197}Au and compare it with existing experimental data (solid circles) [56], at $\theta_n = 1^\circ$. Incidentally, the beam energy for the same experimental data was not unique and was in the range of 36.9 to 44.1 MeV/u. To take care of this variation in our calculation, in Fig. 9 we have shown the neutron energy distribution using the WS (solid line) and AMD (dashed line) wave functions, calculated at a series of beam energies ranging from 37 - 44 MeV/u. In the same figure [Fig. 9(h), dot-dashed line], we have also plotted the average of all the WS results performed at different beam energies.

With the progress in current radioactive ion beam facilities, it would indeed be interesting to perform these exclusive measurements as that could constrain the spread in the data seen in Fig. 9.

3. Parallel momentum distribution

We now turn our attention to the PMD of the charged fragment in the breakup of ^{11}Be on ^{181}Ta at a beam energy of 63 MeV/u. The width of this distribution is also a measure of the size of the nucleus in coordinate space. From a statistical model calculation [57], the width can be given by $\Delta^2 = \Delta_0^2 [A_b(A_a - A_b)/A_a]$, where A_a and A_b are the mass numbers of the projectile and fragment,

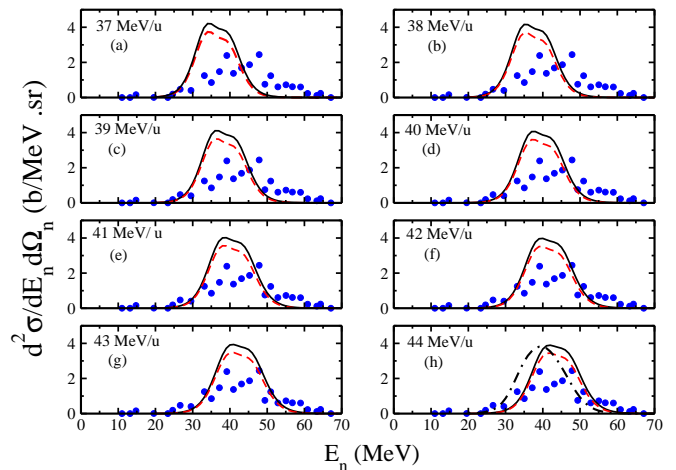


FIG. 9. Neutron energy distributions in the Coulomb breakup of ^{11}Be on a gold target at beam energies ranging from 37 to 44 MeV/nucleon, calculated using WS (solid line) and AMD (dashed line) wave functions. The experimental data are shown by solid circles are from Ref. [56]. In figure (h), the dot-dashed line shows the average of all the WS results performed at different beam energies.

respectively and Δ_0 (≈ 80 MeV/c) has a constant value and it is also known to be independent of target mass and beam energy. This approximation suggests that the width of the ^{10}Be distribution in the breakup of ^{11}Be could be approximately 80 MeV/c. However, the experimental FWHM of the PMD for the s -wave configuration has been found to be 43.6 ± 1.1 MeV/c [58].

In Fig. 10 we show our fully quantum mechanical calculation of the PMD of the charged core (^{10}Be) fragments emitted during the elastic Coulomb breakup of ^{11}Be on ^{181}Ta at a beam energy of 63 MeV/u, in the rest frame of the projectile. The solid and the dashed lines correspond to our calculations with WS and AMD wave functions, respectively and are normalized to the peak of the data. The FWHM for both the theoretical (WS and AMD) calculations are 42 MeV/c which is in good agreement with the experimental value of 43.6 ± 1.1 MeV/c from Ref. [58].

4. Relative energy spectrum and dipole response

We now continue our efforts in testing the WS and the AMD wave functions by calculating the relative energy spectrum and the dipole strength distribution of ^{11}Be on a heavy target. In Fig. 11, we have shown the relative energy spectrum in the elastic Coulomb breakup of ^{11}Be on a ^{208}Pb target at beam energy of 72 MeV/u (upper panel) and dipole strength distribution (lower panel) and compare our results with the available experimental data [15]. The solid and the dashed lines represent FRDWBA calculations using the WS and the AMD wave functions, respectively, while the experimental data are shown by solid circles. We see that both the WS and AMD re-

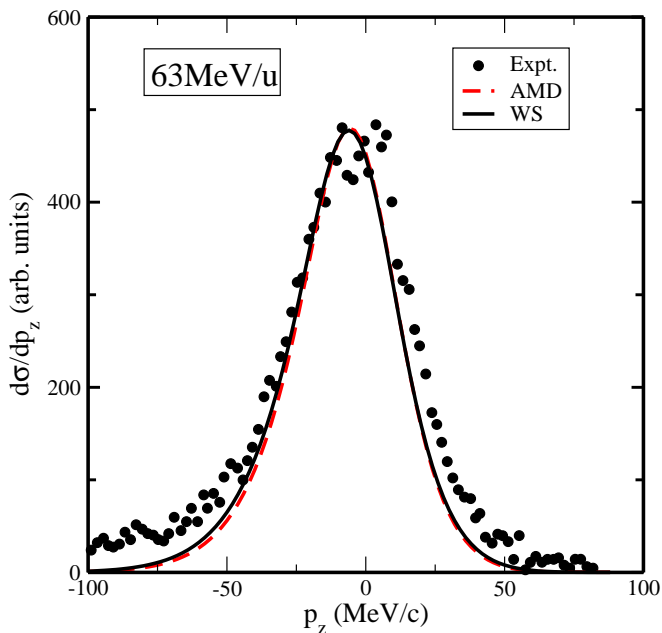


FIG. 10. The parallel momentum (p_z) distribution of ^{10}Be in the elastic Coulomb breakup of ^{11}Be on ^{181}Ta at 63 MeV/u in the rest frame of the projectile. The solid and dashed lines correspond to WS and AMD calculations, respectively and the experimental data, shown by solid circles, are from Ref. [58].

sults are able to reproduce the peak positions of the relative energy spectra and the dipole distribution quite well. Contributions at higher relative energies are dominated by the nuclear breakup [27].

The total one neutron removal cross sections (σ_n), obtained by integrating the relative energy spectrum with the WS and AMD wave functions, are 1.76 b and 1.51 b, respectively and the corresponding experimental value is 1.8 ± 0.4 b [15].

Again the total $B(E1)$ value for ^{11}Be determined experimentally at a beam energy of 72 MeV/u is $1.3 \pm 0.3 e^2 fm^2$ [15] and the theoretical values obtained by integrating the lower panel of Fig. 11 for WS and AMD calculations are 1.17 and $0.97 e^2 fm^2$, respectively. We emphasize that our post form FRDWBA considers the breakup process to be a one-step process [27] and hence the agreement of our calculations with the experimental data is a direct proof that the enhanced dipole strength at low energies is due to the breakup of nucleus into the continuum and not because of any soft dipole resonance. A similar conclusion was also reached by the authors of [52].

Interestingly, in an extreme single-particle model, provided other excited bound states do not contribute to the dipole transition, the total $B(E1)$ is known to be proportional to the mean square radius of the valence nucleon ($\langle r_\nu^2 \rangle$) [19, 20, 59–61], via $B(E1) = (3/4\pi)(Z_a e/A_a)^2 \langle r_\nu^2 \rangle$. Under this approximation, using the theoretical estimates of $B(E1)$ obtained earlier, the root mean square

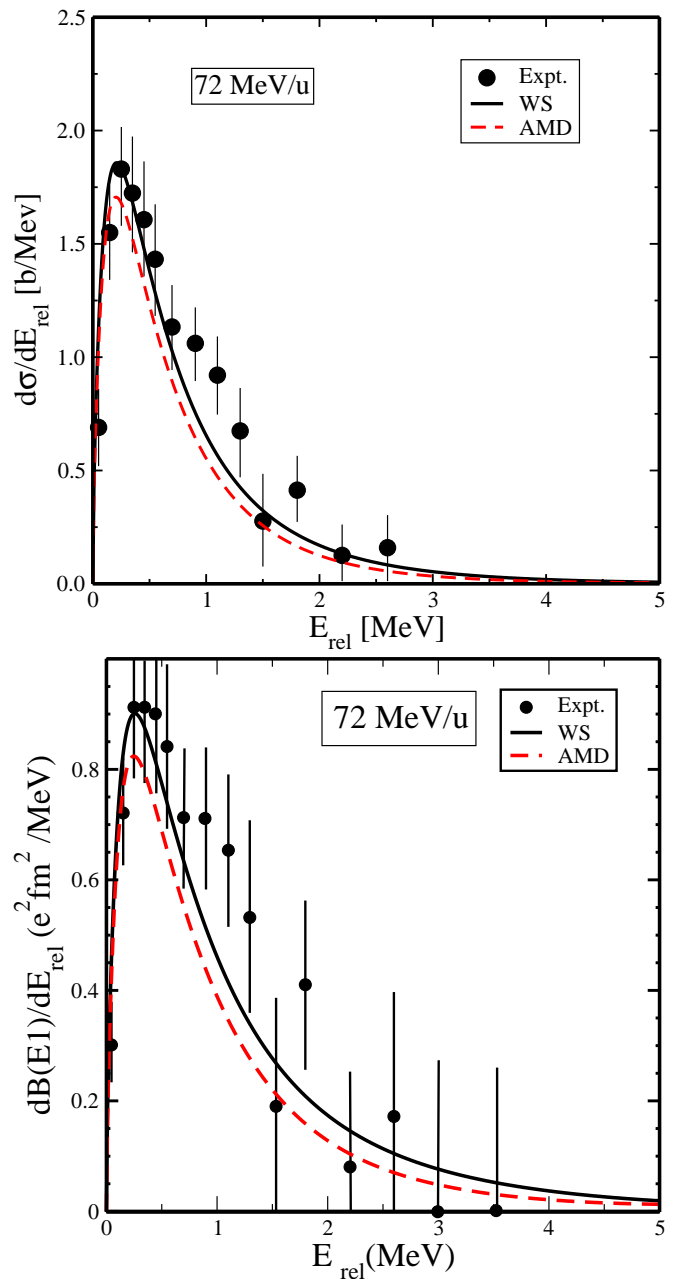


FIG. 11. The relative energy spectra in the elastic Coulomb breakup of ^{11}Be on ^{208}Pb at 72 MeV/u (upper panel) and dipole strength distribution (lower panel). Calculations with the WS and the AMD wave functions are shown by solid and dashed lines, respectively. The solid circles show the experimental data from Ref. [15].

radius of the valence neutron ($\sqrt{\langle r_\nu^2 \rangle}$) with the WS and the AMD wave functions turns out to be 6.08 fm and 5.54 fm, respectively. These do compare well with experimental estimate of 6.4 ± 0.7 fm in Ref. [15].

IV. CONCLUSIONS

We have investigated the static properties and reaction observables of ^{11}Be breaking in the presence of Coulomb field of ^{208}Pb . For our theoretical calculations we have combined the AMD framework and the fully quantum mechanical FRDWBA model.

We have used the AMD to describe the structure and the valence neutron wave function of ^{11}Be . To incorporate the long-ranged asymptotics of the halo wave function, an extended AMD framework named AMD+RGM has also been adopted. The AMD+RGM has drastically improved the asymptotics of halo wave function, and plausibly described various properties such as charge and neutron distribution radii, one neutron separation energy and excitation spectrum.

The valence neutron wave function calculated by AMD+RGM was used as an input of the FRDWBA model to describe the dynamical properties of ^{11}Be . The advantage of the method over other first-order perturbative theories is that it requires only the ground state wave function of the projectile as an input and includes all orders of the electromagnetic interaction between the fragments and the target.

Apart from the many body AMD, a phenomenological Woods-Saxon wave functions has also been used for the purpose of comparison. We have shown that the static properties calculated with these wave functions, mainly

the matter and charge radii of ^{11}Be , are in good agreement with the available data. This gave us the confidence to calculate several reaction observables in the breakup of ^{11}Be on heavy targets. Several observables like the triple differential cross section, neutron energy distribution, parallel momentum distribution, relative energy spectrum and dipole strength distribution are presented and compared with experimental data, wherever available. The upshot of this method is that the same input is used to calculate various exclusive and inclusive observables. Given the validity of our method in the low mass region, it would also be interesting to extend our calculations to the deformed medium mass region of the nuclear chart where experimental data are scarce.

ACKNOWLEDGMENT

This work was supported by the Scheme for Promotion of Academic and Research Collaboration (SPARC/2018-2019/P309/SL), Ministry of Education, India. M.K. acknowledges the support from JSPS KAKENHI Grant No. 19K03859, the collaborative research programs 2020, Information Initiative Center at Hokkaido University and the COREnet program at the RCNP, Osaka University. M.D. acknowledges a doctoral research fellowship from the Ministry of Education, India.

-
- [1] I. Tanihata, *et al.*, Phys. Rev. Lett. **55**, 2676 (1985).
 - [2] Shubhchintak, R. Chatterjee, Phys. Rev. C **90**, 017602 (2014).
 - [3] T. Aumann, T. Nakamura, Phys. Scr., **T152**, 014012 (2013).
 - [4] I. Tanihata, *et al.*, Phys. Lett. B **206**, 592 (1988).
 - [5] W. Nörtershäuser, *et al.*, Phys. Rev. Lett. **102**, 062503 (2009).
 - [6] J. S. Wang, *et al.*, Nucl. Phys. A **691**, 618 (2001).
 - [7] Suhel Ahmed, A. A. Usmani, Z. A. Khan, Phys. Rev. C **96**, 064602 (2017).
 - [8] A. Krieger, *et al.*, Phys. Rev. Lett. **108**, 142501 (2012).
 - [9] C. Forssén, E. Caurier, P. Navrátil, Phys. Rev. C **79**, 021303 (2009).
 - [10] R. E. Warner, *et al.*, Phys. Rev. C **64**, 044611 (2001).
 - [11] P. Capel, *et al.*, J. Phys.: Conf. Ser. **1023**, 012010 (2018).
 - [12] A. Leistenschneider, *et al.*, Phys. Rev. Lett. **86**, 5442 (2001).
 - [13] J. Chambers, *et al.*, Phys. Rev. C **50**, R2671 (1994).
 - [14] Y. Suzuki, K. Ikeda, H. Salto, Prog. Theor. Phys. **83**, 180 (1990).
 - [15] T. Nakamura, *et al.*, Phys. Lett. B **331**, 296 (1994).
 - [16] T. Nakamura, *et al.*, Phys. Rev. Lett. **83**, 1112 (1999).
 - [17] S. Nakayama, *et al.*, Phys. Rev. Lett. **85**, 262 (2000).
 - [18] R. Kanungo, I. Tanihata, C. Samanta, Prog. Theor. Phys. **102**, 1133 (1999).
 - [19] C.A. Bertulani, G. Baur, M.S. Hussein, Nucl. Phys. A **526**, 751 (1991).
 - [20] C.A. Bertulani, A. Sustich, Phys. Rev. C **46**, 6 (1992).
 - [21] S. Goriely, Phys. Lett. B **436**, 10 (1998).
 - [22] C.A. Bertulani, Eur. Phys. J. A **55**, 240 (2019).
 - [23] Y. Kanada-En'yo, M. Kimura, H. Horiuchi, Comptes Rendus Physique **4**, 497 (2003).
 - [24] Y. Kanada-En'yo, M. Kimura, A. Ono, Prog. Theor. Exp. Phys. **2012**, 01A202 (2012).
 - [25] M. Kimura, T. Suhara, Y. Kanada-En'yo, Eur. Phys. J. A **52**, 373 (2016).
 - [26] H. Fuchs, Nucl. Instrum. Methods **200**, 361 (1982).
 - [27] R. Chatterjee, R. Shyam, Prog. Part. Nucl. Phys. **103**, 67 (2018).
 - [28] Manju, J. Singh, Shubhchintak, R. Chatterjee, Eur. Phys. J. A **55**, 5 (2019).
 - [29] J.F. Berger, M. Girod, D. Gogny, Computer Physics Communications **63**, 365 (1991).
 - [30] H. Homma, M. Isaka, M. Kimura, Phys. Rev. **91**, 014314 (2015).
 - [31] M. Kimura, Phys. Rev. C **69**, 044319 (2004).
 - [32] M. Kimura, R. Yoshida, M. Isaka, Prog. Theor. Phys. **127**, 287 (2012).
 - [33] D.L. Hill, J.A. Wheeler, Phys. Rev. **89** 1102 (1953).
 - [34] K. Minomo, T. Sumi, M. Kimura, K. Ogata, Y.R. Shimizu, M. Yahiro, Phys. Rev. C **84**, 034602 (2011).
 - [35] K. Minomo, T. Sumi, M. Kimura, K. Ogata, Y.R. Shimizu, M. Yahiro, Phys. Rev. Lett. **108** 052503 (2012).
 - [36] T. Sumi, K. Minomo, S. Tagami, M. Kimura, T. Matsumoto, K. Ogata, Y.R. Shimizu, M. Yahiro, Phys. Rev. C **85**, 064613 (2012).
 - [37] M. Kimura, Phys. Rev. C **95**, 034331 (2017).

- [38] W. von Oertzen, M. Freer, Y. Kanada-En'yo, Phys. Rep. **432**, 43 (2006).
- [39] W. von Oertzen, II Nuovo Cimento A **110**, 895 (1997)
- [40] W. von Oertzen, Z. Physik A **357**, 355 (1997).
- [41] S. Okabe, Y. Abe, H. Tanaka, Prog. Theor. Phys. **57**, 866 (1979).
- [42] Y. Kanada-En'yo, H. Horiuchi, A. Dote, Phys. Rev. C **64**, 0564304 (1999).
- [43] N. Itagaki, S. Okabe, Phys. Rev. C **61**, 044306 (2000).
- [44] N. Itagaki, S. Okabe, K. Ikeda, I. Tanihata, Phys. Rev. C **64** 014301 (2001).
- [45] Y. Kanada-En'yo, H. Horiuchi, Phys. Rev. C **68**, 014319 (2003).
- [46] T. Neff, H. Feldmeier, R. Roth, Nucl. Phys. A **752**, 321 (2005).
- [47] A. Calci, P. Navrátil, R. Roth, J. Dohet-Eraly, Sofia Quaglioni, Guillaume Hupin, Phys. Rev. Lett. **117**, 242501 (2016).
- [48] A. Bonaccorso, F. Cappuzzello, D. Carbone, M. Caval- laro, G. Hupin, P. Navrátil, S. Quaglioni, Phys. Rev. C **100**, 024617 (2019).
- [49] R. Chatterjee, P. Banerjee, R. Shyam, Nucl. Phys. A **675**, 477 (2000).
- [50] F. M. Nunes, I. J. Thompson, R. C. Johnson, Nucl. Phys. A **596**, 171 (1996).
- [51] B. Zwieglinski, W. Benenson, R.G.H. Robertson, W.R.Coker, Nucl. Phys. A **315**, 124 (1979).
- [52] N. Fukuda, *et al.*, Phys. Rev. C **70**, 054606 (2004).
- [53] A. Mason, R. Chatterjee, L. Fortunato, A. Vitturi, Eur. Phys. J. A **39**, 107 (2009).
- [54] M. Žáková, *et al.*, J. Phys. G. **37**, 055107 (2010).
- [55] J. S. Al-Khalili, J. A. Tostevin, Phys. Rev. Lett. **76**, 3903 (1996).
- [56] R. Anne, *et al.*, Nucl. Phys. A **575**, 125 (1994).
- [57] A. S. Goldhaber Phys. Lett. B **53**, 306 (1974).
- [58] J. H. Kelly, *et al.*, Phys. Rev. Lett. **74**, 30 (1995).
- [59] J. H. Esbensen, G.F. Bertsch, Nucl. Phys. A **542**, 310 (1992).
- [60] M.A. Nagarajan, S. M. Lenzi, A. Vitturi, Eur. Phys. J. A **24**, 63 (2005).
- [61] S. Typel, G. Baur, Nucl. Phys. A **759**, 247 (2005).